Propagation of wind energy into the deep ocean through a fully turbulent mesoscale eddy field.

Eric Danioux, Patrice Klein, Pascal Rivière

Propagation of Wind Energy into the Deep Ocean through a Fully Turbulent Mesoscale Eddy Field

ERIC DANIOUX AND PATRICE KLEIN

Laboratoire de Physique des Océans, IFREMER, Brest, France

PASCAL RIVIÈRE

LEMAR, IUEM, Brest, France

(Manuscript received 10 April 2007, in final form 19 February 2008)

ABSTRACT

The authors analyze the 3D propagation of wind-forced near-inertial motions in a fully turbulent mesoscale eddy field with a primitive equation numerical model. Although the wind stress is uniform, the near-inertial motion field quickly becomes spatially heterogeneous, involving horizontal scales much smaller than the eddy scales. Analysis confirms that refraction by the eddy relative vorticity is the main mechanism responsible for the horizontal distortion of the near-inertial motions, which subsequently triggers their vertical propagation. An important result is the appearance of two maxima of near-inertial vertical velocity (both with rms values reaching 40 m day^{-1}): one at a depth of 100 m and another unexpected one much below the main thermocline around 1700 m. The shallow maximum, captured by the highest vertical normal modes, involves near-inertial motions with a spatial heterogeneity close to the eddy vorticity gradient field. These characteristics match analytical results obtained with Young and Ben Jelloul's approach. The deep maximum, captured by the lowest vertical normal modes, involves superinertial motions with a frequency of twice the inertial frequency and much smaller horizontal scales. Because of these characteristics, not anticipated by previous analytical studies, these superinertial motions may represent an energy source for small-scale mixing through a mechanism not taken into account in the present study: the parametric subharmonic instability (PSI). This reveals a pathway by which wind energy may have a significant impact on small-scale mixing in the deep interior. Further studies that explicitly take into account PSI are needed to estimate this potential impact.

1. Introduction

Contribution of wind energy to the deep ocean mixing is discussed by Wunsch and Ferrari (2004). Using Alford's (2003) results, these authors (see also Munk and Wunsch 1998) suggest that wind-driven near-inertial energy (with frequency close to the Coriolis frequency) could sustain the small-scale mixing in the deep interior, needed to resupply the available potential energy removed by the overturning and mesoscale eddy generation. But how this energy penetrates into the ocean interior is still a puzzle. In this paper, we demonstrate that the presence of mesoscale oceanic eddies favors rapid penetration of wind-forced near-inertial oscillations (NIOs) into the ocean interior with characteristics propitious to mixing.

One important effect of mesoscale oceanic eddies on wind-forced NIOs is to reduce their horizontal scales (initially large because of the wind scales), which is a preliminary condition for their vertical propagation (Gill 1984). Kunze (1985) argues that the eddy relative vorticity polarizes NIOs, expelling them from cyclonic structures and trapping them within anticyclonic ones within a few inertial periods. The β effect also reduces the NIOs' length scale (D'Asaro 1989; Garrett 2001) but is not as efficient as relative vorticity in fully turbulent eddy fields: in such fields, vorticity gradients have rms values as large as $10^{-10} - 10^{-9}$ m^{-1} s^{-1}, that is, one to two orders of magnitude larger than the β value ($\approx 1.6 \times 10^{-11}$ m^{-1} s^{-1} at midlatitudes). Other studies (Plougonven and Snyder 2005; Straub 2003) point out the effects of the eddy deformation field (instead of the

Corresponding author address: Patrice Klein, LPO, IFREMER, BP 70, 29280 Plouzané, France.
E-mail: pklein@ifremer.fr

DOI: 10.1175/2008JPO3821.1

eddy relative vorticity field) as an efficient mechanism for the dispersion of NIOs. However, experimental and analytical studies by D'Asaro (1995), Young and Ben Jelloul (1997, hereafter YBJ), and Klein et al. (2004) confirm Kunze's results. A further quantification of the vertical propagation of NIOs has been attempted in some numerical studies such as those by Klein and Tréguier (1995), Van Meurs (1998), Lee and Niiler (1998), Balmforth et al. (1998), and Zhai et al. (2005). But these studies consider idealized jets or a few eddies with specific length scales. Consequently, a better understanding of NIOs vertical propagation within a fully turbulent mesoscale eddy field (i.e., characterized by a continuous wavenumber spectrum) is still needed. Relevance of such a study comes from the coincidence of regions with strong mesoscale variability in both the atmosphere and the ocean at midlatitudes (Zhai et al. 2005).

In the present paper, we use numerical simulations with a primitive equation model to analyze and characterize the 3D propagation of wind-forced NIOs embedded in a fully turbulent eddy field. Our analysis makes use of the normal-mode framework (Gill 1984) and the analytical approach of Young and Ben Jelloul (1997) as a guideline to rationalize the numerical results. The advantage of the YBJ approach compared with Wentzel–Kramers–Brillouin (WKB) theory is that it does not assume a priori any scale separation between NIOs and the background mesoscale flow. As such, it is more appropriate when both fields, as in our study, are characterized by a continuous wavenumber spectrum. Moreover, the resemblance and departure of our numerical results with/from analytical solutions obtained with the YBJ approach will allow better identification of the mechanisms that drive vertical propagation of NIOs in the ocean. The next section presents a review of the YBJ approach, and section 3 describes the numerical simulations performed. Sections 4 and 5 discuss the results in both physical and spectral spaces. Section 4 more specifically concerns the 3D propagation of near-inertial horizontal kinetic energy, whereas section 5 describes the 3D propagation of near-inertial vertical kinetic energy. A discussion and conclusions are proposed in section 6.

2. A review of Young and Ben Jelloul's approach

The penetration of NIOs into the ocean interior can be understood within the framework of the normal-mode analysis detailed in Gill (1984). Expansion of u, v, and w, the horizontal and vertical near-inertial velocity components, in terms of the vertical normal modes leads to

$$(u, v) = \sum_{n=0}^{\infty} (u_n, v_n)(x, y, t) F_n(z), \tag{1}$$

$$w = \sum_{n=1}^{\infty} \left(\frac{\partial u_n}{\partial x} + \frac{\partial v_n}{\partial y} \right)(x, y, t) H_n(z), \tag{2}$$

with t being the time and x, y, and z the horizontal (zonal and meridional) and vertical coordinates. The F_n are the eigenfunctions of the classical Sturm–Liouville problem (Flierl 1978):

$$\mathcal{L}F_n = -\frac{1}{r_n^2} F_n. \tag{3}$$

Here, $\mathcal{L}$ is the differential operator defined as $\mathcal{L}(\cdot) = \partial/\partial z[f^2/N^2 \partial/\partial z(\cdot)]$, with N the Brunt–Väisälä frequency. Here r_n is the Rossby radius of deformation of mode n, and $H_n(z)$ is given by $H_n(z) = \int_z^0 F_n(z')dz'$. The functions H_n constitute an orthogonal basis for the scalar product $(H_n H_m) = \int_{-H}^0 N^2 H_n H_m \, dz$. Equation (2) uses the continuity equation.

Using the framework of the normal-mode analysis, Young and Ben Jelloul (1997) studied the 3D dispersion of NIOs in a fully turbulent eddy field. Their procedure filters out the inertial period and studies the slower subinertial evolution of the complex amplitude $\mathcal{A}$ of the NIOs defined as

$$u + iv = \mathcal{A} e^{-ift}, \tag{4}$$

where $i^2 = -1$ and f is the Coriolis frequency. This approach does not assume any horizontal scale separation between NIOs and the background mesoscale flow, which allows obtaining analytical solutions when both fields are characterized by continuous horizontal wavenumber spectra. However, in its simplest form, it assumes a vertical scale separation between NIOs and eddy fields. Furthermore, only the eddy relative vorticity is supposed to play a role in the dispersion of the NIOs, that is, the effects of the eddy strain ($\partial u/\partial x - \partial v/\partial y$) and shear ($\partial u/\partial y + \partial v/\partial x$) deformation fields are not considered. Finally, wave–wave nonlinear interactions are assumed to be weak.

The simplest equation for $\mathcal{A}$ derived by YBJ is (see also Klein et al. 2004)

$$\frac{\partial \mathcal{L}\mathcal{A}}{\partial t} + i\frac{\zeta}{2}\mathcal{L}\mathcal{A}_0 + \frac{i}{2} f \nabla^2 \mathcal{A} = 0, \tag{5}$$

with $\mathcal{A}_0$ being the initial value of $\mathcal{A}$ (assumed uniform, i.e., independent of x and y), ζ is the eddy relative vorticity, and ∇^2 is the horizontal Laplacian operator. The second term on the left-hand side is related to the refraction of NIOs by eddy relative vorticity: it shifts the phase of NIOs but does not affect their amplitude. The

third term is related to the horizontal dispersion of NIOs. NIOs' vertical propagation is implicitly taken into account by the operator $\mathcal{L}$, which affects only the first and second terms. Better physical insight of (5) is obtained when this equation is further simplified, using

$$\mathcal{A}(x, y, z, t) = \sum_{n=0}^{\infty} \mathcal{A}_n(x, y, t) F_n(z)$$

and (3). Equation (5) then becomes an equation that drives the time evolution of $\mathcal{A}_n$. Subsequent analysis using

$$\mathcal{A}_n = \mathcal{R}_n e^{i\theta_n}, \tag{6}$$

with $\mathcal{R}_n$ being the amplitude and θ_n the phase of the nth mode; defining $\mathcal{R}'_n$ and θ'_n as small departures of $\mathcal{R}_n$ and θ_n from the initially uniform values $\mathcal{R}_{0n}$ and θ_{0n} (i.e., $\mathcal{R}'_n = \mathcal{R}_n - \mathcal{R}_{0n}$ and $\theta'_n = \theta_n - \theta_{0n}$) leads to the resulting linearized coupled equations:

$$\frac{\partial \theta'_n}{\partial t} = -\frac{\zeta}{2} + \frac{D_n}{2} \frac{\nabla^2 \mathcal{R}'_n}{\mathcal{R}_{0n}} \quad \text{and} \tag{7}$$

$$\frac{\partial \mathcal{R}'_n}{\partial t} = -\mathcal{R}_{0n} \frac{D_n}{2} \nabla^2 \theta'_n, \tag{8}$$

where $D_n = r_n^2 f$ can be interpreted as a "dispersivity parameter" and is analogous to the diffusivity associated with passive scalar diffusion processes (Metzger 1999). The first term on the right-hand side of (7) represents the shift of the phase of NIOs by eddy relative vorticity. The right-hand side of (8) is related to the horizontal dispersion of the phase of NIOs, whereas the second term on the right-hand side of (7) is related to the horizontal dispersion of the amplitude of NIOs. Equation (7) shows that at earlier times, ζ first affects the phase of NIOs such that $\theta'_n \approx -\zeta t/2$. Then dispersion (8) can work and the amplitude $\mathcal{R}'_n$ approaches the Laplacian of the eddy vorticity (i.e., $\mathcal{R}'_n \approx D_n t^2 \mathcal{R}_{0n} \nabla^2 \zeta / 8$) with its amplitude positive (negative) in anticyclonic (cyclonic) structures. These solutions at earlier times are close to those obtained by Kunze (1985) and Klein and Tréguier (1995).

Because the eddy field is usually characterized by a continuous wavenumber spectrum, an exact solution of (7)–(8) in physical space at a later time is difficult to obtain directly. Using classical spectral properties of the oceanic mesoscale eddy field, Klein et al. (2004) derived an estimate of the solution of (7)–(8) in physical space at any time t (see the appendix). Their solution for $\mathcal{R}'_n$ concerns scales larger than a critical length scale l_{cn} given by

$$l_{cn} = \sqrt{2\pi D_n t}. \tag{9}$$

The critical wavenumber associated with this length scale is

$$k_{cn} = \sqrt{\frac{2\pi}{D_n t}}. \tag{10}$$

Here, l_{cn} corresponds to the most energetic scale of the nth mode of NIOs.[1] Their solution in physical space is

$$\frac{\mathcal{R}'_n}{\mathcal{R}_{0n}} = \max\left(\frac{D_n t^2}{8} \nabla^2 \zeta_{cn}, -1\right), \tag{11}$$

with $\nabla^2 \zeta_{cn}$ being the horizontal Laplacian of the eddy vorticity field truncated so as to retain only horizontal scales larger than l_{cn}. The analytical solution (11) is valid only when the horizontal wavenumber spectrum of the eddy relative vorticity has a slope gentler than k^{-4} (see the appendix).

Lowest vertical normal modes (with large r_n and D_n) disperse faster than higher ones because their group velocity, proportional to r_n and therefore to D_n, is larger [see also the coefficient in front of t^2 in Eq. (11)]. These modes involve larger scales than higher ones because of the larger value of l_{cn}. Consequently, the different vertical modes should quickly decorrelate, making NIOs penetrate into the ocean interior.

3. Primitive equation simulations

a. The mesoscale eddy field

The mesoscale eddy field used in our study results from the nonlinear baroclinic instability of a large-scale westerly jet in a zonal β-plane channel centered at 45°N. The parameter setting resembles that used by Karsten et al. (2002) and Rivière et al. (2004). Characteristics of the numerical simulation are close to those in Lapeyre and Klein (2006). The domain size is 1000 km × 2000 km, and its depth is 4000 m. The numerical resolution is 6 km on the horizontal and involves 33 levels on the vertical with a vertical grid spacing ranging from 5 m near the surface to 500 m near the bottom. A biharmonic operator is used for the horizontal viscosity and diffusion with an appropriate coefficient of -0.5×10^9 m^4 s^{-1}. Vertical diffusion is parameterized using Mellor and Yamada's (1982) 2.5 model. The Brunt–Väisälä frequency (Fig. 1a) involves a main thermocline around 600 m deep. The F_n eigenfunctions (the barotropic mode is not shown), defined by (3), display maxima located in the upper layers (Fig. 1b), whereas

[1] Because the dispersivity parameter D_n is analogous to a diffusivity, a physical interpretation is that l_{cn} is the length scale over which the near-inertial amplitude is dispersed in time t.

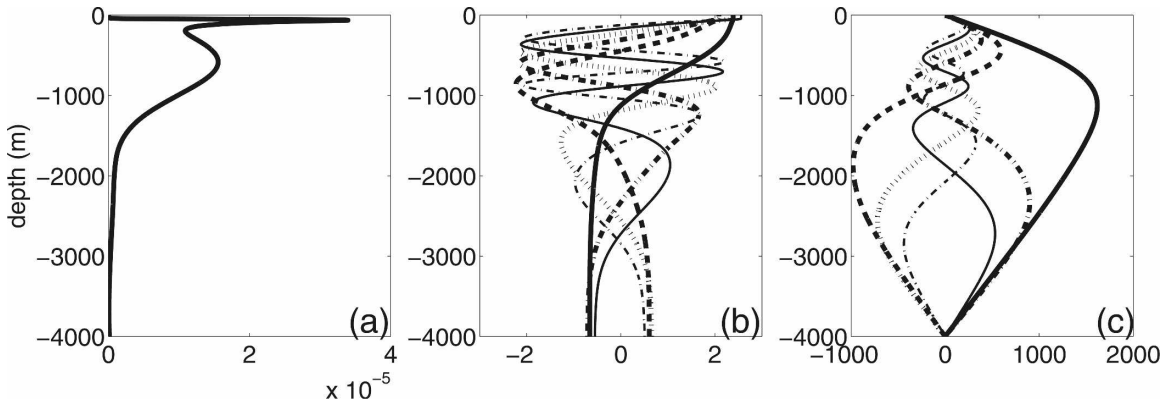

FIG. 1. (a) Vertical profiles of N^2, (b) the first six eigenfunctions F_n given by Eq. (3), and (c) the first six functions H_n. Units in (a) are s^{-2}.

the functions H_n (Fig. 1c) display maxima in the deeper layers. The first four Rossby radii of deformation are 24, 10, 7, and 5 km, respectively. Because of the vertical resolution, vertical normal modes for $n \geq 13$ are not well resolved. The mesoscale eddy field is forced using a relaxation of the zonally averaged velocity and density fields to the initial state. While adjusting the mean zonal flow, such forcing does not damp the eddy field.

After a spinup of 300 days, the total eddy kinetic energy (integrated over the whole domain) equilibrates, not varying much during the subsequent 300 days. The rms Rossby number associated with the equilibrated eddy field is $\mathrm{Ro} = \sqrt{\langle \zeta^2 \rangle}/f_0 \approx 0.10$, where $\langle \cdot \rangle$ is a horizontal average, ζ is the eddy relative vorticity, and f_0 is the Coriolis frequency at the center of the domain. Relative vorticity reaches values as strong as 0.4 f_0 near the surface. As depth increases, the rms Rossby number slowly decreases to 0.02 at 800 m. Using $W/H = \sqrt{\langle (\boldsymbol{\nabla}_\mathrm{H} \cdot \boldsymbol{u}_\mathrm{H})^2 \rangle}$, the omega equation, and the thermal wind balance, one shows that $W/H = V^2 f_0 / H^2 N^2 = f_0 \mathrm{Ro}^2 \mathrm{Bu}^{-1}$, so that the Burger number $\mathrm{Bu} = \mathrm{Ro}^2 f_0 / \sqrt{\langle (\boldsymbol{\nabla}_\mathrm{H} \cdot \boldsymbol{u}_\mathrm{H})^2 \rangle} \approx 2.4$. The mesoscale eddy field is therefore close to quasigeostrophic assumptions—in particular, it has time scales much larger than the Coriolis period. A 60-m-thick surface mixed layer is then created as the result of strong solar radiation first acting alone, then compensated for by a surface cooling of the same amplitude (such that the net surface heat forcing is zero) for 15 days. This accounts for the peak of the Brunt–Väisälä frequency near 100 m as shown in Fig. 1a.

Figure 2a shows a snapshot of the surface density field at the end of the spinup period. This field is characterized by large-scale meridional gradients. The surface streamfunction Ψ (not shown) at the same time displays a large-scale meridional structure corresponding to the large-scale zonal jet in thermal wind balance with the density field, and mesoscale eddies with a di-

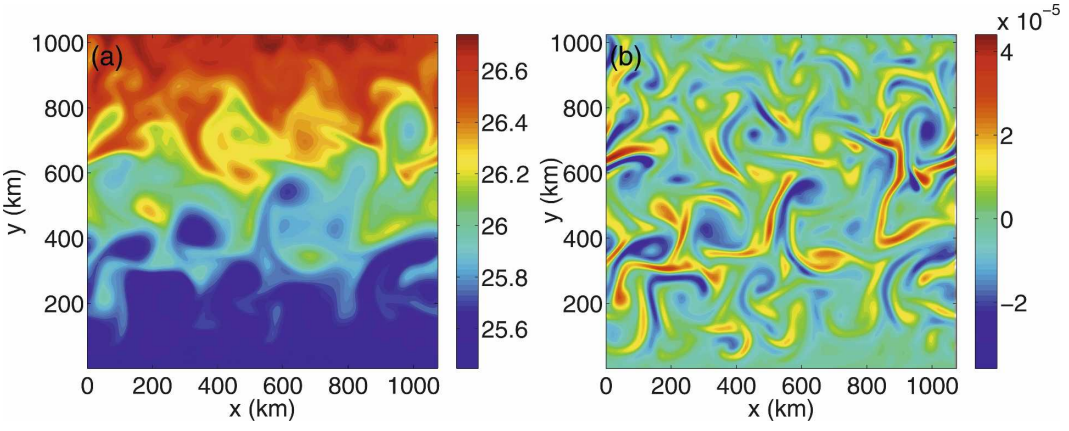

FIG. 2. Snapshots of the (a) surface density anomaly (g cm^{-3}) and of the (b) surface relative vorticity (s^{-1}) of the equilibrated mesoscale eddy field.

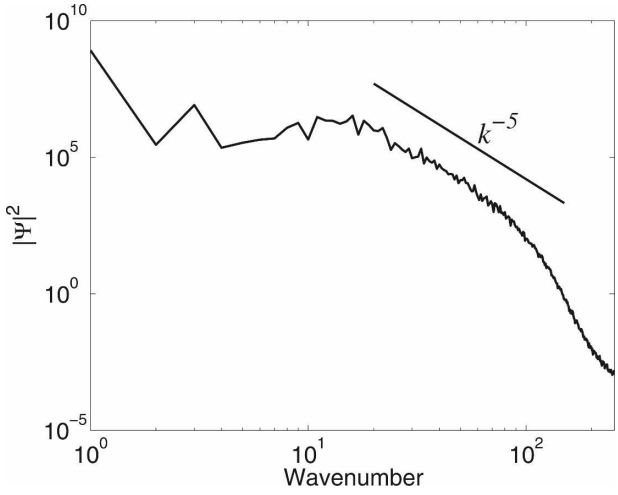

FIG. 3. Horizontal wavenumber spectrum of the surface streamfunction $\Psi = \nabla^{-2}\zeta$ at equilibrium. Wavenumbers are nondimensionalized, and $k = 10$ represents a wavelength of 390 km. Units for $|\Psi|^2$ are $m^4\ s^{-2}$.

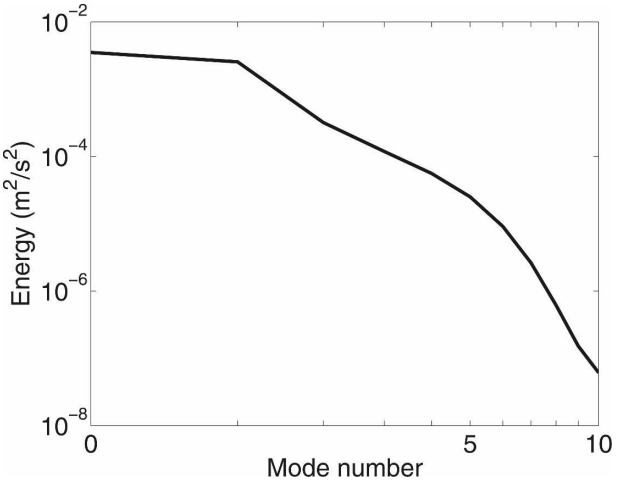

FIG. 4. Vertical-mode spectrum of the mesoscale eddy velocity at equilibrium. Mode 0 corresponds to the barotropic mode.

ameter between 150 and 300 km. Its horizontal wavenumber spectrum (Fig. 3) is characterized by a slope close to k^{-5} within the wavenumber range 10–100 (in nondimensional units $k = 10$ represents a wavelength of 390 km). This means that the surface relative vorticity field has a k^{-1} spectrum slope within this spectral range. In physical space, the relative vorticity (Figs. 2b) exhibits smaller-scale structures than the streamfunction and the density, including small-scale vortices and wavy, thin filaments. Decomposition of the eddy motions onto vertical normal modes using (2) leads to the vertical-mode spectrum displayed in Fig. 4. The mesoscale eddy field is mainly captured by the barotropic mode (mode 0) and the first baroclinic mode (mode 1), with the barotropic mode dominating.

b. The atmospheric forcing

We study the response of the ocean to a resonant wind forcing in the presence of mesoscale eddies. The chosen forcing consists of a wind of constant amplitude rotating clockwise at the inertial frequency during one inertial period, then stopped:

$$\tau(t) = \tau_0 \times \begin{cases} \exp(-ift) & \text{for } 0 < t \le \dfrac{2\pi}{f_0}, \\ 0 & \text{for } t > \dfrac{2\pi}{f_0}, \end{cases} \tag{12}$$

with $\tau = \tau_x + i\tau_y$ being the surface wind stress. The magnitude τ_0 (equal to $5 \times 10^{-4}\ m^2\ s^{-2}$) corresponds to a wind speed of 16 m s^{-1}. This forcing is uniform over the whole domain.

This resonant wind is similar to the passage of an occluding midlatitude atmospheric cyclone. Furthermore, it provides a maximum wind energy input to the ocean in a short time and ensures that the Ekman transport is zero. Wind-driven NIOs are confined to the mixed layer at the end of the wind pulse. Because this forcing is uniform, NIOs' amplitude is uniform after the wind pulse.

c. The near-inertial motion field

A wind-forced numerical simulation has been performed for 10 inertial periods using the wind pulse described in the preceding section. The initial state is the equilibrated mesoscale eddy field described in section 3a. For comparison, a second simulation, identical to the previous one but without wind forcing, has been run. Figure 5 shows the average horizontal and vertical kinetic energy profiles with and without wind forcing.

Analysis of the near-inertial motion requires separating the high-frequency motions (here, NIOs) from the low-frequency ones associated with the mesoscale eddies because the numerical model calculates the total field. To that purpose, we used two methods. The first makes use of a low-pass filter to get the low-frequency field $\overline{X}$ of any variable X:

$$\overline{X}(t) = \frac{1}{T_f} \int_{t-\frac{T_f}{2}}^{t+\frac{T_f}{2}} X\, dt, \tag{13}$$

with $T_f = 2\pi/f_0$ being the Coriolis period. The high-frequency motion field in this case is the difference between the total and low-frequency fields. This method implicitly assumes that the time variation of the

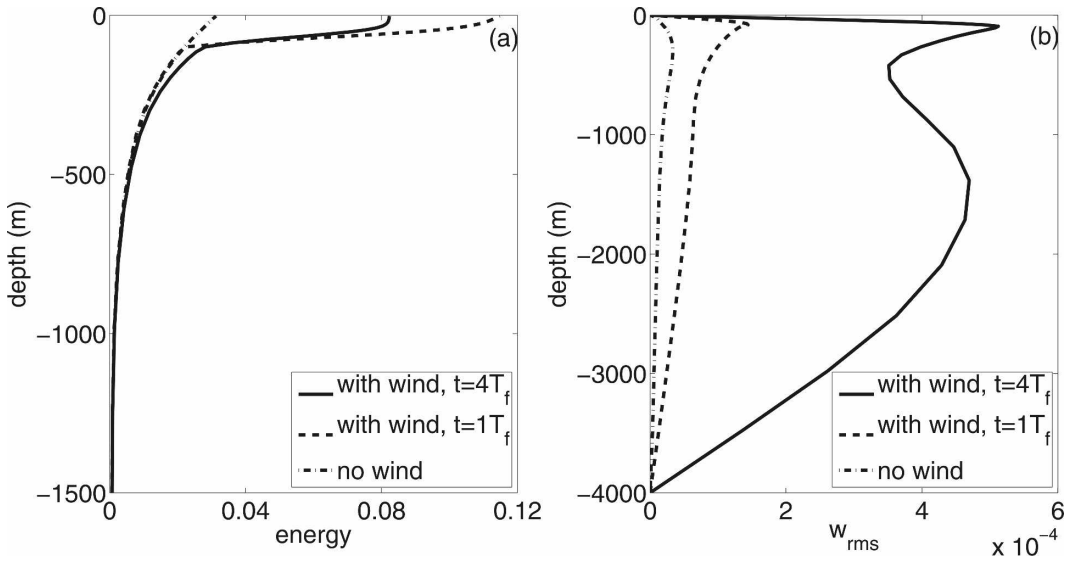

FIG. 5. (a) Vertical profiles of the horizontal kinetic energy averaged over the whole horizontal domain and (b) rms of the vertical velocity (defined as $\sqrt{\langle w^2 \rangle}$, where $\langle \cdot \rangle$ is the horizontal average operator). Dotted–dashed curves are the profiles without wind forcing, and dashed and solid curves are the profiles with wind forcing at $t = 1$ and 4 IP, respectively. Note: $t = 1$ IP represents the time just after the wind pulse. Units are $m^2 s^{-2}$ in (a) and $m s^{-1}$ in (b).

low-frequency flow is small over an inertial period, which appears reasonable because the Rossby number of this flow is small (Ro $\approx$ 0.1). The second method takes advantage of the absence of an Ekman transport for the wind forcing used and consists of subtracting the instantaneous 3D field obtained with wind forcing from the one obtained without wind forcing. It implicitly assumes that NIOs have no effect on the eddy flow and have no other sources than the wind. As shown in Fig. 6, near-inertial fields obtained with the two methods are very similar. Last, the comparison (detailed in the next section) of the extracted near-inertial field with the analytical solutions of Klein et al. (2004) confirms a posteriori the efficacy of these separation methods for the wind forcing used.

The difference between the profiles with and without wind forcing (Figs. 5a,b) is a good approximation of the kinetic energy associated with the near-inertial motions. At $t = 1$ inertial period (IP), the near-inertial horizontal kinetic energy is trapped within the mixed layer (Fig. 5a). During the next three inertial periods, this energy slowly propagates downward as deep as 500 m. On the other hand, the differences between the vertical kinetic energy with and without wind forcing (Fig. 5b) display an unexpected time increase and a large depth penetration of near-inertial vertical kinetic energy. The magnitude of the rms of the near-inertial vertical velocity increases by a factor more than 5 within three inertial periods (cf. the dashed and solid profiles in Fig. 5b). In addition to a maximum at 100 m, its vertical propagation is characterized by the rapid emergence of a maximum near 1700 m, attaining a depth as large as 3000 m at $t = 4$ IP. At that time, the

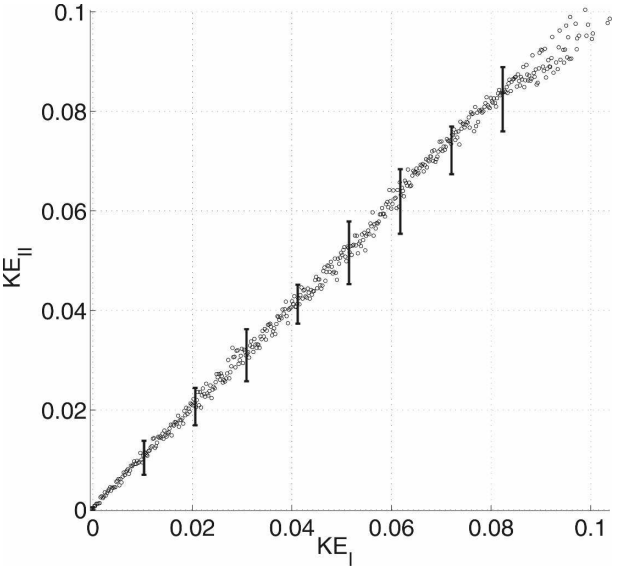

FIG. 6. Scatterplot between near-inertial horizontal kinetic energy (in $m^2 s^{-2}$) obtained with the first method (KE_I) and with the second method (KE_{II}) at the surface at $t = 4$ IP. Each point represents the average over each grid point on the abscissa (which has a total of 500 grid points), and vertical lines show std dev around the averages.

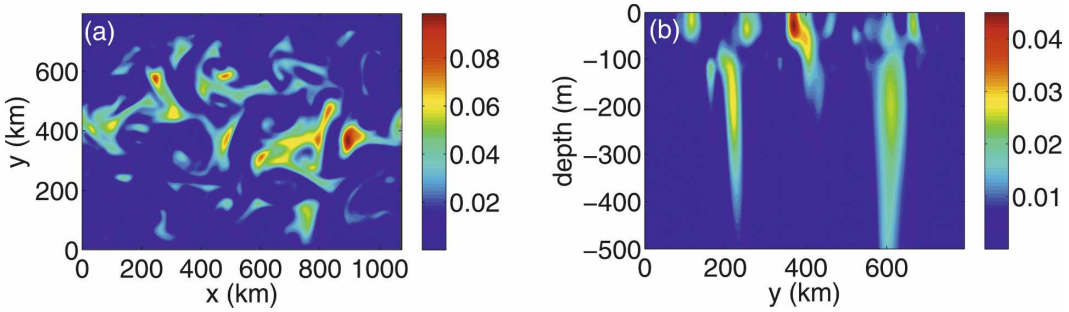

FIG. 7. Snapshots at $t = 9$ IP of the near-inertial horizontal kinetic energy ($m^2 s^{-2}$) (a) at the surface and (b) along a meridional vertical section.

magnitude of the deep maximum is as large as that of the upper maximum (at 100 m) and is almost 10 times larger than that associated with the mesoscale eddy field. Note that near-inertial horizontal velocities are not strictly homogeneous at the end of the wind pulse. Although their amplitude is still uniform, their phase is already affected by the eddy vorticity, which explains the existence of near-inertial vertical velocities close to the mixed layer base at $t = 1$ IP. Near-inertial vertical kinetic energy stops increasing after 8 IP.

Near inertial horizontal kinetic energy slowly decreases after the wind pulse: the ratio of near-inertial horizontal kinetic energy to mesoscale kinetic energy decreases from 0.36 just after the wind pulse down to 0.24 after 10 inertial periods. A detailed kinetic energy budget shows that this decrease is due to the numerical horizontal viscosity. This mixing is small for mesoscale eddies, but it becomes significant for the near-inertial horizontal motions because their spatial heterogeneity involves energetic small scales (see section 4). While near-inertial vertical kinetic energy strongly increases after the wind pulse, its magnitude is still three orders smaller than near-inertial horizontal kinetic energy.

4. Near-inertial horizontal kinetic energy

Although almost uniform and trapped within the 60-m-thick mixed layer just after the wind pulse, near-inertial horizontal motions quickly become spatially heterogeneous, involving horizontal scales much smaller than the eddy scales (Fig. 7a) and significant vertical propagation into the ocean interior (Fig. 7b) down to 1000 m. The vertical penetration (Fig. 8), deeper in negative vorticity regions (Fig. 8b) than in positive ones (Fig. 8c), highlights the eddy vorticity effects. There is a remarkable similarity between Fig. 8b herein and Figs. 5b–d in Lee and Niiler (1998), which emphasizes the chimney effect of the eddies. A more detailed diagnosis of the complex distribution of the near-inertial motion field is difficult to undertake without using some analytical guidelines. Consequently, YBJ's approach (described in section 2) is used hereafter to analyze our results.

When near-inertial horizontal motions are decomposed onto vertical normal modes following (1), the vertical-mode spectrum (Figs. 9) reveals a clear time evolution of their organization linked to the eddy rela-

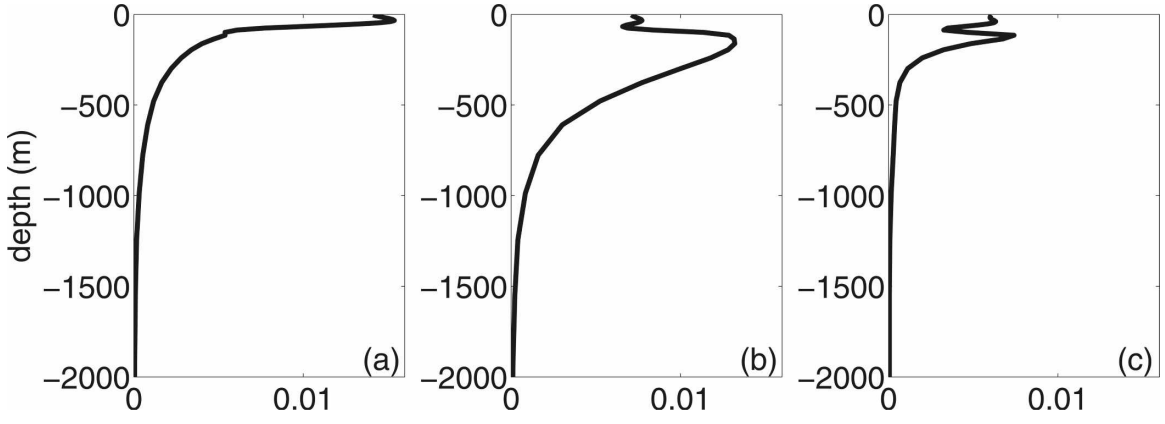

FIG. 8. Vertical profiles at $t = 9$ IP of the near-inertial horizontal energy in $m^2 s^{-2}$ (a) averaged over the whole domain, (b) averaged over areas where the surface relative vorticity $\zeta < -2 \times 10^{-5}\ s^{-1}$, and (c) averaged over areas where $\zeta > -2 \times 10^{-5}\ s^{-1}$.

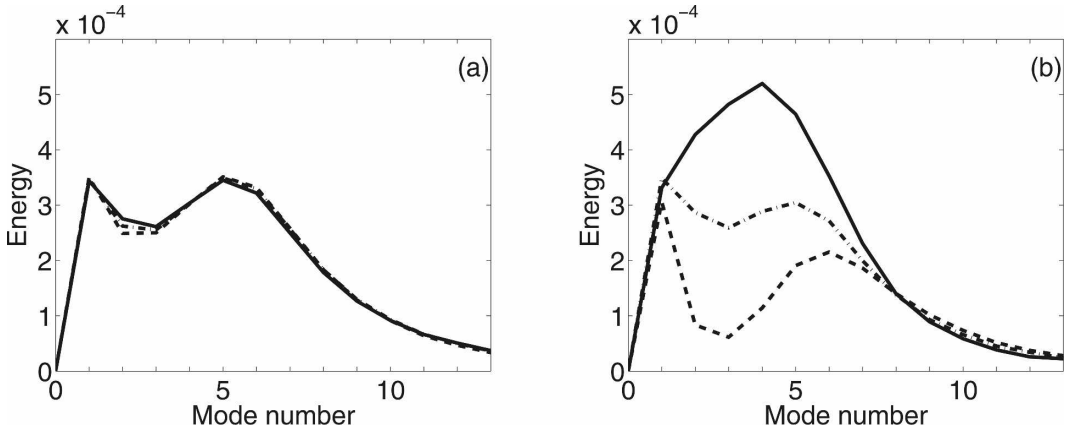

FIG. 9. Vertical-mode spectrum of the near-inertial horizontal velocity field ($\sqrt{u^2 + v^2}$) at (a) $t = 1$ IP and (b) $t = 4$ IP in regions where $\zeta < -2 \times 10^{-5}$ s^{-1} (solid lines), $\zeta > 2 \times 10^{-5}$ s^{-1} (dashed lines), and -2×10^{-5} s$^{-1} < \zeta < 2 \times 10^{-5}$ s^{-1} (dotted–dashed lines). Units on the vertical axis are m^2 s^{-2}.

tive vorticity. At $t = 1$ IP (i.e., just after the wind pulse), NIOs have the same vertical normal-mode spectrum in all regions, whatever the eddy vorticity sign (Fig. 9a). This mode spectrum is dominated by the first and fifth baroclinic modes. The barotropic mode (mode 0) is negligible. Such results indicate that interaction between the mesoscale eddy field and NIOs principally involves the barotropic mode of the eddy field (which is the dominant mode) and the baroclinic modes of the NIOs. The first baroclinic mode of the eddy field should have a much weaker influence on the NIOs. The main reason (see Flierl 1978) is that our stratification varies with depth, and, consequently, triple interaction coefficients between vertical normal modes are less than 0.02 when the barotropic mode is not involved.

Numerical results reveal the following evolution. At $t = 2$ IP, the vertical-mode spectrum (not shown) reveals that the first baroclinic mode has larger (smaller) amplitude in negative (positive) vorticity regions, higher baroclinic modes almost being not affected. This indicates that the first mode has been expelled from cyclonic structures and trapped within anticyclonic ones. At that time, all the vertical modes (including the first one) have their phase correlated with the eddy vorticity field (not shown). At $t = 4$ IP, Fig. 9b reveals that the spectral amplitude of the intermediate modes (modes 2 to 7) is smaller in cyclonic regions and larger in anticyclonic ones, indicating that these modes have been expelled in turn from cyclonic structures and trapped within anticyclonic ones. Higher-mode amplitudes are not affected yet. The phase of the intermediate and higher modes at $t = 4$ IP (see modes 5 and 10 in Fig. 10) is significantly correlated with the eddy vorticity field as anticipated by Klein et al. (2004) using the

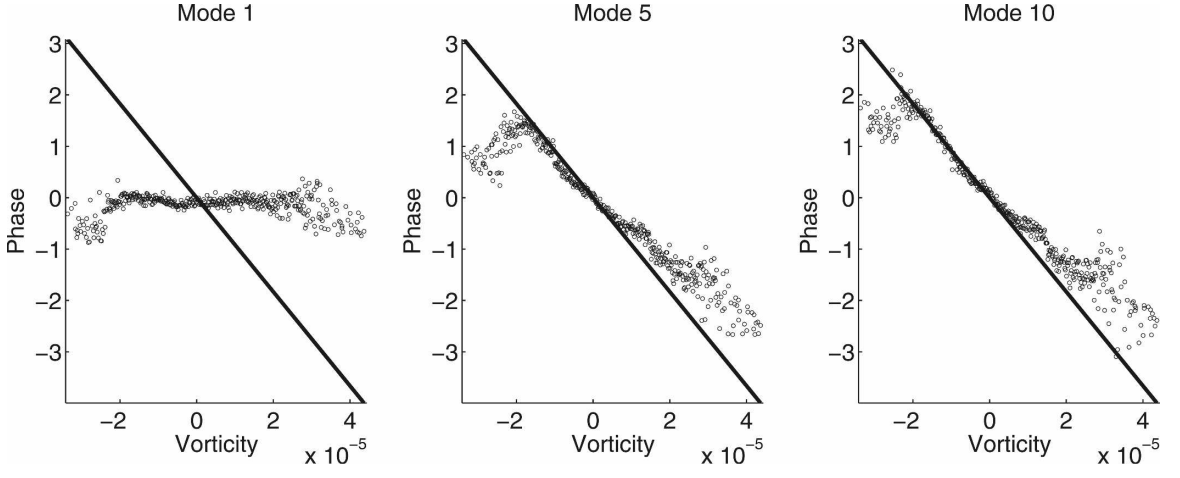

FIG. 10. Scatterplot at $t = 4$ IP of the phase θ of modes 1, 5, and 10 of the NIOs with the relative vorticity of the eddy field. Solid line correspond to the analytical solution at earlier times $\theta = -\zeta t/2$.

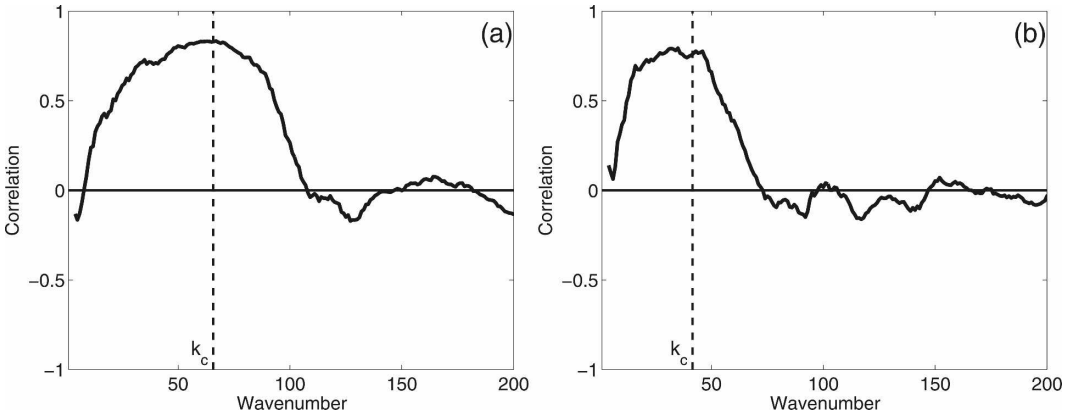

FIG. 11. Correlation between spectral coefficients (averaged along circular rings in horizontal wavenumber space) of the near-inertial horizontal energy of mode 3 and the Laplacian of the (a) surface relative vorticity $\nabla^2\zeta$ at $t = 2$ and (b) 5 IP. The critical horizontal wavenumber $k_c = \sqrt{2\pi/D_3 t}$ is represented by a dashed line. Wavenumbers are in nondimensional units and $k = 10$ represents a wavelength of 390 km.

YBJ approach (see section 2 and the appendix). On the other hand, the lowest-mode (mode 1) amplitude does not reveal a dependence on the eddy vorticity sign anymore (Fig. 9b). Its phase (see mode 1 in Fig. 10) has become scrambled and is no longer correlated to the eddy vorticity field.

To further understand whether eddy relative vorticity drives the time evolution of the vertical normal modes of NIOs as predicted by analytical results obtained with the YBJ approach, we have compared the amplitude of the vertical normal modes given by (11) with the one observed in our simulations. As discussed in section 2, (11) indicates that for a given vertical normal mode n, near-inertial energy should resemble the Laplacian of the vorticity field truncated so as to retain only scales larger than the critical length scale $l_{cn} = \sqrt{2\pi D_n t}$.

Let us focus on the third vertical normal mode. Figures 11a,b reveal that as time goes on, the near-inertial horizontal kinetic energy of mode 3 remains well correlated to the Laplacian of the eddy vorticity field for horizontal wavenumbers lower than $k_{c3} = 2\pi/l_{c3}$, with k_{c3} decreasing with time [as given by (10)]. For higher wavenumbers the correlation quickly drops to zero. Moreover, the kinetic energy spectrum of mode 3 (Fig. 12b) reveals an energy maximum for a wavenumber

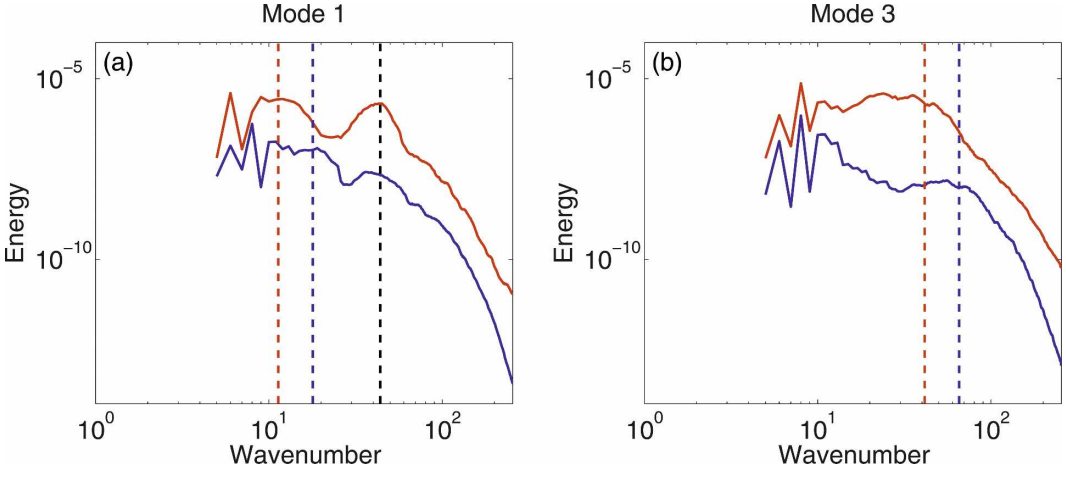

FIG. 12. Horizontal wavenumber spectra at $t = 2$ (blue) and 5 (red) IP of the amplitudes of modes (a) 1 and (b) 3. For clarity, the spectrum at $t = 5$ IP is shifted by a decade. The theoretical wavenumber $k_c = \sqrt{2\pi/(D_n t)}$ is represented by blue (for $t = 2$ IP) and red (for $t = 5$ IP) dashed vertical lines. The black dashed vertical line appearing in (a) corresponds to the wavenumber $\sqrt{3}/r_1$, with r_1 being the Rossby radius of deformation of mode 1. Wavenumbers are in nondimensional units, and $k = 10$ represents a wavelength of 390 km.

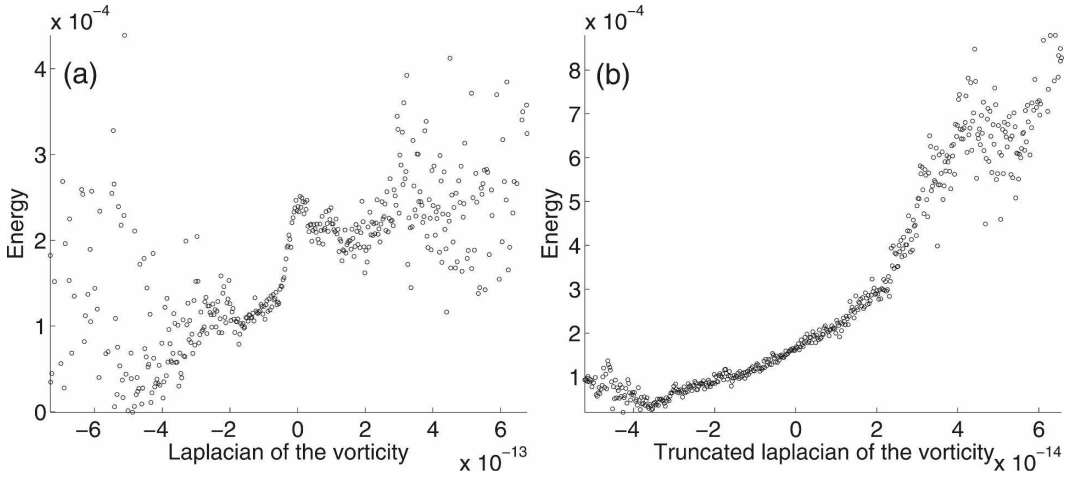

FIG. 13. Scatterplot at $t = 5$ IP (a) of the near-inertial horizontal energy (in $m^2\ s^{-2}$) of mode 3 with the Laplacian of the surface vorticity $\nabla^2\zeta$ (in $m^{-2}\ s^{-1}$) and (b) of the near-inertial horizontal energy of mode 3 with the Laplacian of the surface vorticity truncated $\nabla^2\zeta_{c3}$ so as to retain scales larger than $l_{c3} = \sqrt{2\pi D_3 t}$.

close to the critical wavenumber k_{c3} (dashed vertical line). Figure 13 further confirms this agreement with the analytical solution (11). From Fig. 13a, the near-inertial energy associated with mode 3 at $t = 5$ IP does not seem to be correlated to the total Laplacian of the vorticity field $\nabla^2\zeta$. However, when $\nabla^2\zeta$ is truncated so as to retain only scales larger than $l_{c3} = \sqrt{2\pi D_3 t}$, it appears well correlated to the near-inertial energy (Fig. 13b). Results for higher modes display an even better agreement with the analytical solution (11), the critical length scale being smaller for these modes because of their smaller Rossby radius of deformation.

On the contrary, results for the lower modes (modes 1 and 2—mode 0 is not energetic) depart from the analytical solution (11). Although the kinetic energy spectrum of the first baroclinic mode (Fig. 12a) displays a peak at a wavenumber close to the critical wavenumber k_{c1} at $t = 2$ and $t = 5$ IP, a second peak located at a higher wavenumber $k = \sqrt{3}/r_1$, with r_1 being the first Rossby radius of deformation, appears and increases with time. This second peak, almost as energetic as the first one at $t = 5$ IP, is not anticipated by the analytical solution (11). The near-inertial kinetic energy spectrum associated with the second baroclinic mode (not shown) also displays a second peak but at the wavenumber $k = \sqrt{3}/r_2$, with r_2 being the second Rossby radius of deformation.

Thus, the time evolution of NIOs embedded in a fully turbulent eddy field is partly understandable when these motions are decomposed onto vertical normal modes and analyzed using the YBJ approach. The dynamics of the higher modes ($n \geq 3$) at any time, and of the lowest modes (modes 1 and 2) at an earlier time, follow the analytical solutions described in section 2 (which a posteriori corroborates the choice of the methods used to extract the near-inertial signal, described in section 3c). This confirms that these modes are principally distorted by eddy relative vorticity, not by the eddy deformation field. Their horizontal dispersion, characterized by the length scale l_{cn}, is much larger for the lower vertical normal modes than for the higher ones because of their larger Rossby radius of deformation. However, the behavior of the lowest modes, which are the fastest to disperse, significantly differs at later times from the analytical solution (11). We suspect that for these modes, nonlinear interactions between NIOs become significant (see section 5a and Danioux and Klein 2008). Because of the different dispersion and time evolution of the vertical normal modes, near-inertial motions propagate from the upper layers into the ocean interior.

5. Near-inertial vertical kinetic energy

Characteristics of the near-inertial vertical kinetic energy (highlighted by the difference between the profiles with and without wind in Fig. 5b) differ from those of the near-inertial horizontal kinetic energy. Just after the wind pulse, near-inertial vertical kinetic energy exhibits a maximum around 100 m, characterized by a strong spatial heterogeneity with small horizontal scales, but its rms magnitude is still weak. The horizontal wavenumber spectrum (not shown) at that time displays a plateau that extends down to scales as small as 40 km. At later times, the vertical kinetic energy penetrates into the ocean interior more quickly and deeply than the horizontal kinetic energy, with its magnitude increasing with time. As mentioned in section 3c, at $t =$

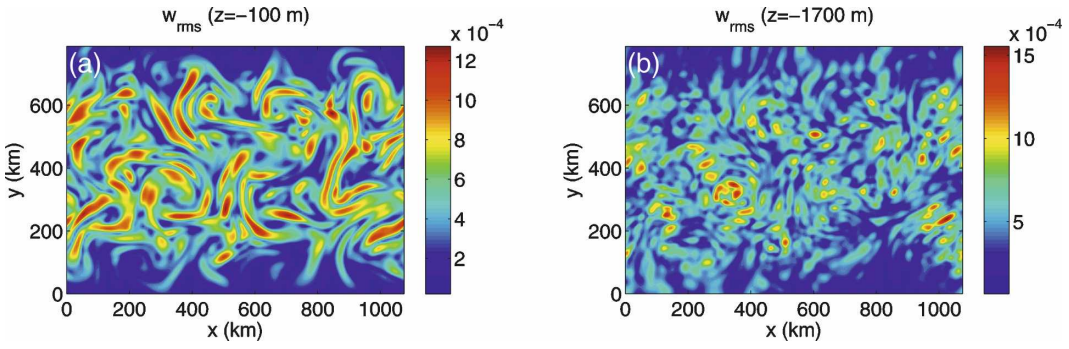

FIG. 14. Snapshots at $t = 6$ IP of the temporal rms value of the vertical velocity (in m s^{-1}), i.e., $w_{\rm rms} = \sqrt{\overline{w^2}}$ (where the overbar represents the temporal mean over one inertial period), at (a) $z = -100$ m and (b) $z = -1700$ m.

4 IP, it displays two maxima, one around 100 m and another around 1700 m, with similar rms values on the order of 40 m day^{-1} and extrema of 100 m day^{-1} (Fig. 5b).

a. *Characteristics of the two w maxima of the near-inertial motions*

The w field at 100 m at $t = 4$ IP (Fig. 14a) contains small-scale, elongated structures, with a width on the order of 50 km. Its horizontal wavenumber spectrum (Fig. 15a) has a shape resembling that observed just after the wind pulse with a plateau extending down to scales as small as 40 km. The w field at 1700 m (Fig. 14b) is dominated by patchy structures with smaller scales than at 100 m. Its horizontal wavenumber spectrum (Fig. 15b) displays a narrow peak that corresponds to a wavelength of 90 km and a secondary peak at 36 km.

The normal-mode analysis [using (2)] of the near-inertial vertical velocity field reveals that the maximum at 100 m is mainly captured by the higher vertical modes (modes 4 to 12) (cf. Figs. 16c,a), while the maximum at 1700 m is captured by the three lowest vertical modes (cf. Figs. 16b,d). These specific vertical-mode contributions, together with the results of section 4, explain the characteristics of these two maxima.

Because the w field at 100 m is mainly captured by the higher modes (modes 4–12), which have been found in the preceding section to follow the analytical solutions of the YBJ approach, the w field at 100 m should follow the analytical solution (A5) detailed in the appendix and should be close to the horizontal gradient of the eddy relative vorticity field. These characteristics have been checked in our numerical simulations. The spectral correlation displayed in Fig. 17b clearly indicates that the spatial heterogeneity of the contribution of mode 8 (i.e., w_8) resembles the vorticity gradient

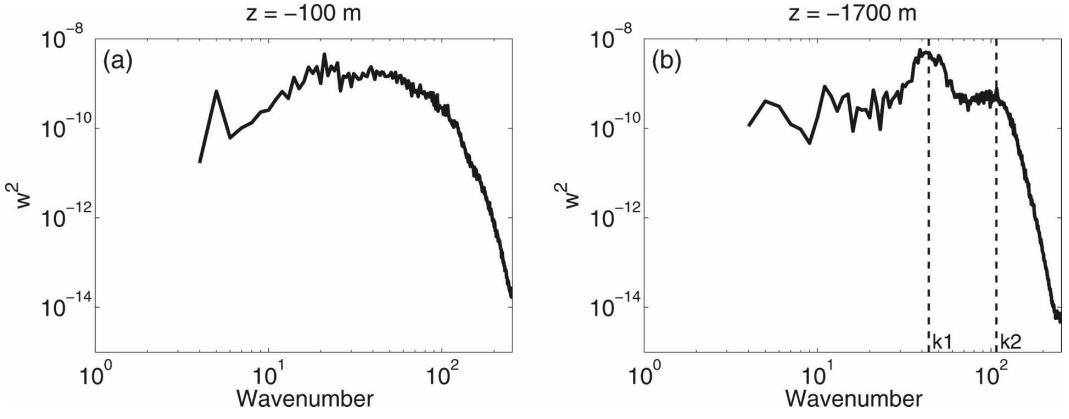

FIG. 15. Horizontal wavenumber spectrum at $t = 6$ IP of w at (a) $z = -100$ m and (b) $z = -1700$ m. Values of $k_1 = \sqrt{3}/r_1$ and $k_2 = \sqrt{3}/r_2$ are indicated. Wavenumbers are in nondimensional units, and $k = 10$ represents a wavelength of 390 km. Units on the vertical axis are m^2 s^{-2}.

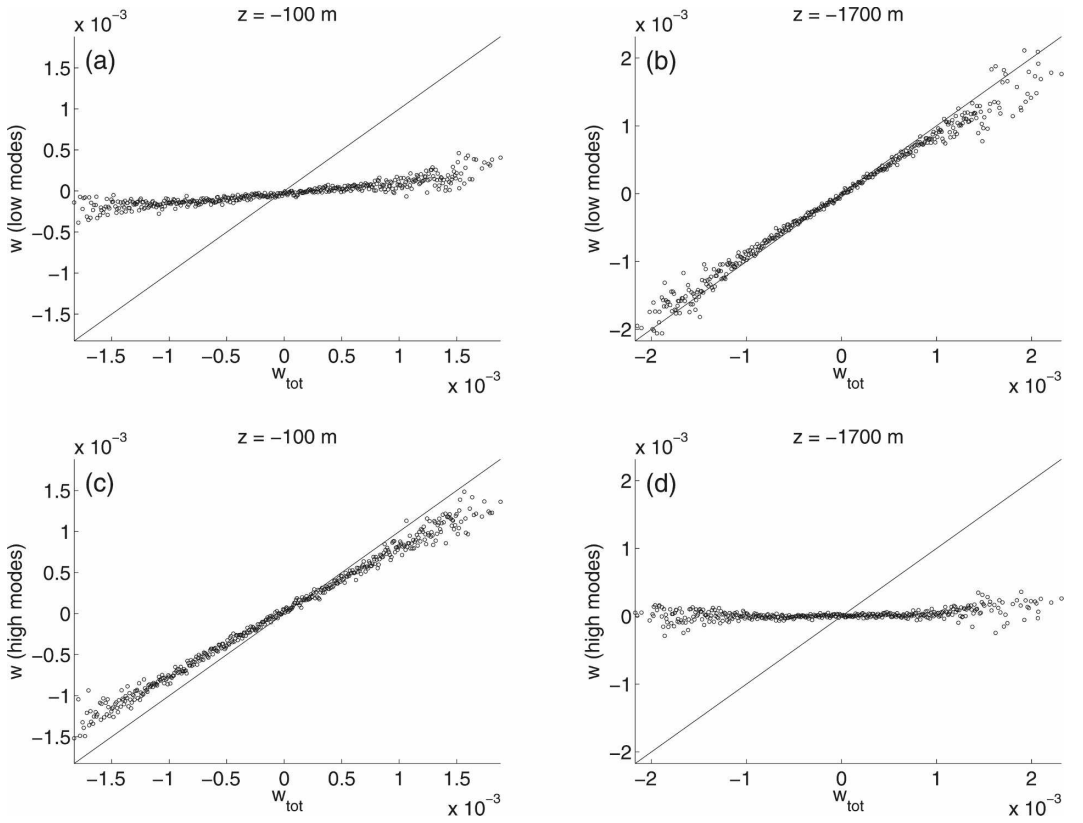

FIG. 16. Scatterplots at $t = 6$ IP of the total near-inertial vertical velocity (w_{tot}) with the (a), (b) low vertical normal modes' contribution (modes 1 to 3) and with the (c), (d) higher vertical normal modes' contribution (modes 4 to 12) at (a), (c) $z = -100$ m and (b), (d) $z = -1700$ m. Velocities are in m s^{-1}.

field. The same result is obtained for the other high modes (modes 4–12) and for the total w field at 100 m (not shown). The similarities between the horizontal wavenumber spectrum of w at 100 m (Fig. 15a) and the higher-mode wavenumber spectra (see mode 6 in Fig. 19b) confirm these characteristics. The frequency spectrum shows that the w field at 100 m (dashed line on Fig. 18) mostly oscillates at the inertial frequency.

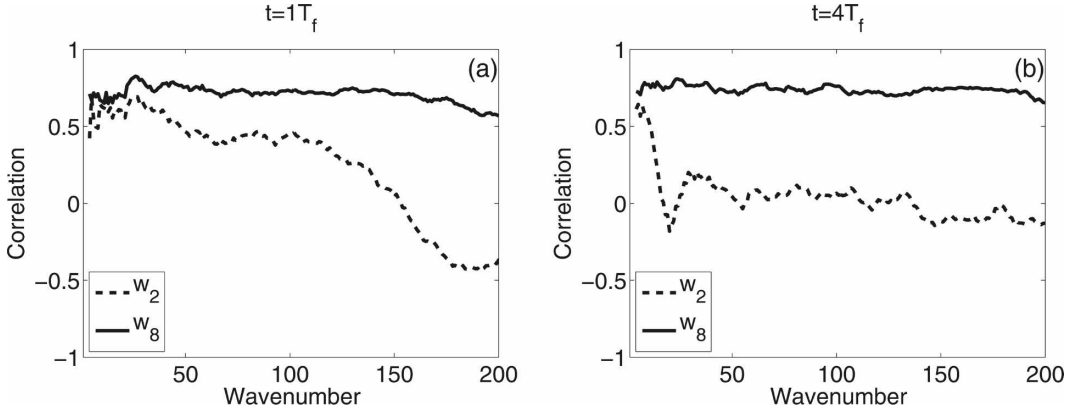

FIG. 17. Correlation coefficient between spectral coefficients (averaged along circular rings in horizontal wavenumber space) of the amplitude averaged over one inertial period of w_2 (dashed line) or w_8 (solid line) with the eddy vorticity gradient, at (a) $t = 1$ IP and (b) $t = 4$ IP. Wavenumbers are in nondimensional units, and $k = 10$ represents a wavelength of 390 km.

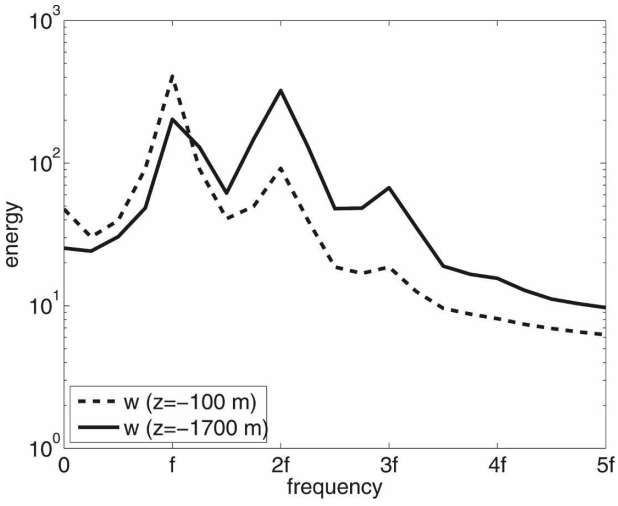

FIG. 18. Frequency spectrum at $t = 6$ IP of w at $z = -100$ m (dashed line) and $z = -1700$ m (solid line).

The w field at 1700 m (Fig. 14b) is captured by the lowest vertical modes (modes 1–3) that have been found in section 4 (in particular, modes 1 and 2) to depart from the analytical solutions of the YBJ approach. Such departure is confirmed by Fig. 17b: at $t = 4$ IP, if the second baroclinic mode of the near-inertial vertical velocity w_2 followed the analytical solution (26), it should be correlated with the vorticity gradient field for wavenumbers $k \leq k_{c2}$, with $k_{c2} = 31$ in nondimensional units [multiply by $2\pi/(3.9 \times 10^6)$ m^{-1} to get the dimensional wavenumbers]. But the correlation, represented by the dashed curve, falls to zero at $k = 17$. The same departure (not shown) from the YBJ approach has been found for the first mode of the w field. These differences with the analytical solution explain the existence of two narrow dominant peaks on the w spectrum at 1700 m (Fig. 15b). The first peak is also present on the horizontal spectrum of the first baroclinic mode (Fig. 19a) and is located at the wavenumber $k_1 = \sqrt{3}/r_1$, with r_1 being the Rossby radius of deformation of the first baroclinic mode. This peak does not appear on the spectra of the other vertical normal modes. The secondary peak clearly emerges in the spectrum of mode 2 (not shown) but is not present in other spectra. It corresponds to the wavenumber $k_2 = \sqrt{3}/r_2$, with r_2 being the Rossby radius of deformation of mode 2. These two specific wavenumbers (k_1 and k_2) have already been identified in section 4. Another feature of the w field at 1700 m, not anticipated by the analytical results, concerns its frequency spectrum. This spectrum (solid line on Fig. 18) reveals that the dominant frequency is twice the inertial frequency. Secondary peaks are present at f and $3f$. Frequency spectra of modes 1 and 2 of the near-inertial vertical velocity (not shown) also display a dominant peak at $2f$. In a companion note (Danioux and Klein 2008), it is shown that the departure of these lowest modes from the analytical solution (26) is due to a resonance mechanism specific to each mode, which does not need to involve other modes. In this mechanism, for a given baroclinic mode, eddy relative vorticity excites, through the nonlinear terms ignored in the YBJ approach, inertia-gravity waves of frequency $2f$ and wavenumber $k = \sqrt{3}/r$, with r being the Rossby radius of deformation of the mode considered. Because of the properties of the vorticity spectrum, this resonance appears essentially for modes 1 and 2.

These characteristics, in particular the kinetic energy peaks at frequencies equal to or larger than twice the inertial frequency, may have important consequences, which are discussed in section 6.

b. *Explanation of the appearance of the deep maximum*

The preceding results for the vertical velocity field, in terms of vertical normal-mode decomposition, and the results of section 4 lead to proposing a simple explanation for the emergence of the deep maximum. From (2), the vertical velocity variance can be written as

$$\langle w^2 \rangle = \left\langle \left(\sum_{n=1}^{\infty} w_n H_n \right)^2 \right\rangle = \sum_n \langle w_n^2 \rangle H_n^2 + \sum_{n \neq m} \langle w_n w_m \rangle H_n H_m, \tag{14}$$

where

$$w_n = \frac{\partial u_n}{\partial x} + \frac{\partial v_n}{\partial y} \tag{15}$$

and $\langle \cdot \rangle$ is the average operator over the whole horizontal domain. The w_n directly depends on the time evolution of u_n and v_n, as described in section 4.

Just after the wind pulse, near-inertial horizontal velocities are trapped within the mixed layer. At that time, dispersion has not worked yet, so the amplitude of the near-inertial velocities is still homogeneous. But their phase is affected by the eddy relative vorticity. The solution at this short time for each mode n can be written as

$$(u_n, v_n)(t') = u_{n0} \left[\cos\left(f + \frac{\zeta}{2}\right)t', -\sin\left(f + \frac{\zeta}{2}\right)t' \right] F_n(z), \tag{16}$$

and

$$w_n = -\frac{t' |\nabla_H \zeta|}{2} u_{n0} \sin\left[\left(f + \frac{\zeta}{2}\right)t' + \alpha \right], \tag{17}$$

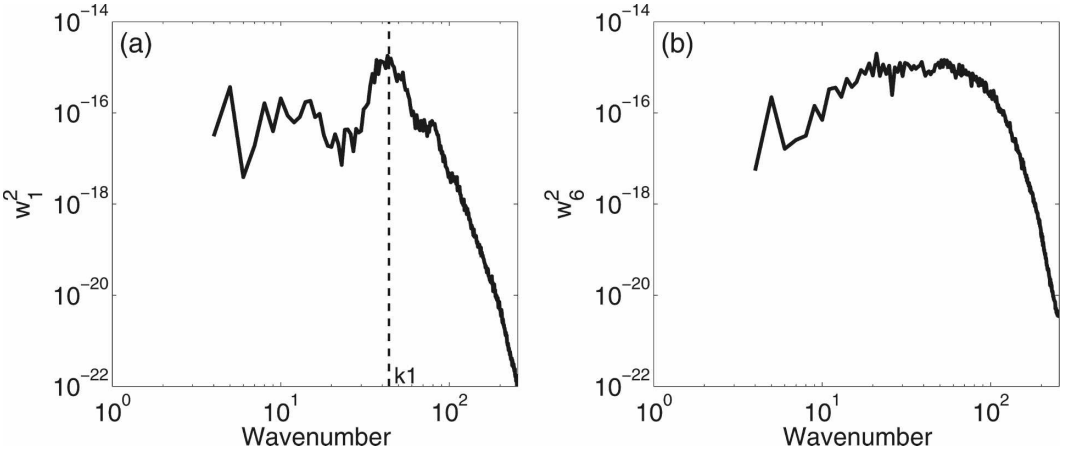

FIG. 19. Horizontal wavenumber spectrum at $t = 4$ IP of vertical modes (a) w_1 and (b) w_6. The value $k_1 = \sqrt{3}/r_1$ is indicated. Wavenumbers are in nondimensional units, and $k = 10$ represents a wavelength of 390 km. Units on the vertical axis are $m^2\ s^{-2}$.

with u_{n0} being the initially homogeneous amplitude of mode n. Here, $t' = 0$ represents the time just after the wind pulse. The horizontal vorticity gradient is written as $(\partial\zeta/\partial x, \partial\zeta/\partial y) = |\nabla_H\zeta|(\cos\alpha, \sin\alpha)$. The subinertial part of (17) is similar to (A5). The expression for the total near-inertial vertical velocity variance is

$$\langle w^2\rangle = \left\langle \left\{ \frac{t'|\nabla_H\zeta|}{2} \sin\left[\left(f+\frac{\zeta}{2}\right)t' + \alpha\right]\right\}^2 \right\rangle \left(\sum_{n=1}^{\infty} u_{n0}H_n\right)^2. \tag{18}$$

The left part of the right-hand side of (18) is the dependence with time and horizontal coordinates of $\langle w^2\rangle$, whereas the right part represents its vertical structure. Equation (18) reveals that a short time after the wind pulse, the amplitude of the vertical velocity is related to the horizontal vorticity gradient and increases linearly with time. The vertical structure of $\langle w^2\rangle$ is represented by the dotted–dashed curve in Fig. 20a, where $(t'|\nabla_H\zeta|/2)\sin[(f + \zeta/2)t' + \alpha]$ has been replaced by a constant a for simplicity. This structure presents a maximum near the base of the mixed layer, which is understandable because near-inertial horizontal velocities are trapped within the mixed layer at this time.

Later, vertical motions associated with the first baroclinic mode (i.e., w_1) disperse and are no longer correlated with the eddy vorticity gradient, whereas higher modes, not yet dispersed, are still close to the eddy vorticity gradient field [see solution (A5)]. Moreover, because of the resonance mechanism described in sec-

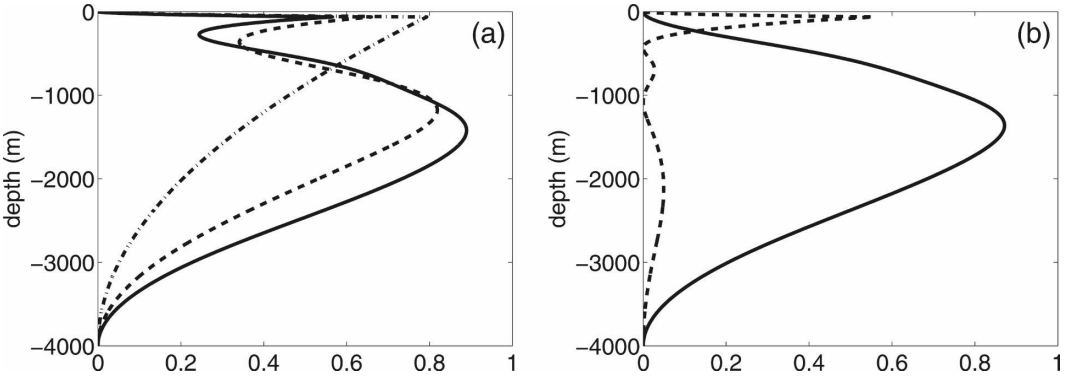

FIG. 20. (a) Vertical profile of $\langle w^2\rangle$ when all vertical modes are correlated [dotted–dashed profile, which corresponds to (18)], when mode 1 is decorrelated from the other modes [dashed profile, which corresponds to (19)], and when both modes 1 and 2 are decorrelated from the other modes [solid profile, which corresponds to (20)]. (b) Specific contributions to the solid profile in (a) of modes 1 and 2, i.e., $\langle w_1^2\rangle H_1^2 + \langle w_2^2\rangle H_2^2$ (solid curve), and of the higher modes, i.e., $\langle(\Sigma_{n\geq 3} w_n H_n)^2\rangle$ (dashed curve). These profiles are obtained using $w_n = a u_{n0}$ in (18), (19), and (20) with a being a constant and u_{n0} the projection on mode n of the initial near-inertial horizontal velocity.

tion 5a, w_1 quickly develops energy at the specific wavenumber $k_1 = \sqrt{3}/r_1$. This means that w_1 differs from w_n at that time, and therefore that $\langle w_1 w_n \rangle \approx 0$ for $n \geq 2$. In this case, $\langle w^2 \rangle$ can be written as

$$\langle w^2 \rangle \approx \langle w_1^2 \rangle H_1^2 + \left\langle \left(\sum_{n \geq 2} w_n H_n \right)^2 \right\rangle. \tag{19}$$

If we use again $w_n = a u_{n0}$ for simplicity (with a being a constant) in (19), we get the vertical profile for $\langle w^2 \rangle$ represented by the dashed line in Fig. 20a. This profile exhibits two maxima: one at 100 m and another around 1200 m.

Later still, the second baroclinic mode becomes decorrelated from the eddy relative vorticity gradient (as illustrated in Fig. 17b) and therefore from the higher modes. The resulting additional decorrelation $\langle w_2 w_n \rangle \approx 0$ with $n \geq 3$ leads to the expression

$$\langle w^2 \rangle \approx \langle w_1^2 \rangle H_1^2 + \langle w_2^2 \rangle H_2^2 + \left\langle \left(\sum_{n \geq 3} w_n H_n \right)^2 \right\rangle. \tag{20}$$

This expression produces a deeper maximum in the interior, as shown in Fig. 20a by the solid profile. Its depth is now closer to that exhibited by the solid profile in Fig. 5b. This simple explanation indicates that the decorrelation between low and high vertical normal modes is responsible for the appearance of a strong maximum of near-inertial vertical velocities in the deep interior. This decorrelation is due to effects of the eddy relative vorticity on the lowest vertical modes that differ from those on higher modes because of their different Rossby radius of deformation. When the respective mode contributions to these new profiles are plotted (Fig. 20b), it immediately appears that the shallower maximum is explained by higher modes and the deeper one by lower modes, which explains the scatterplots displayed in Fig. 16.

6. Discussion and conclusions

The 3D propagation of wind-forced NIOs, embedded in a fully turbulent mesoscale eddy field, has been analyzed within a vertical normal-mode framework and using YBJ's approach as a guideline. This choice has allowed us to explain the physics involved, in particular the rapid time evolution and dispersion of the NIOs field as well as its characteristic length scales. Although the near-inertial motion field is initially uniform, it quickly becomes spatially heterogeneous with horizontal scales much smaller than the eddy scales and experiences a significant vertical propagation into the ocean interior. Analysis indicates that the effect of the relative vorticity associated with the eddy field is the main mechanism that drives this propagation. The eddy strain and shear deformation field does not appear to have any influence. The additional assumptions on which the YBJ linear approach is based have been successfully verified, at least for the higher vertical normal modes ($n \geq 3$) of near-inertial motions: for these modes, wave–wave interactions are negligible during the simulation duration. The lowest modes (modes 1 and 2) that disperse more rapidly appear to saturate after a few inertial periods because of wave–wave interactions.

The faster evolution of the lowest vertical modes and their different characteristics make them decorrelate quickly from higher ones. As a result, two maxima of near-inertial vertical velocities appear after the wind pulse, one around 100 m and another one much below the main thermocline around 1700 m. The shallower maximum principally involves higher vertical modes, whereas the deeper one involves the lowest vertical modes (Fig. 16). The characteristics of the shallower maximum are close to those anticipated by the YBJ analytical approach. At this level, the vertical velocity field has a frequency close to the inertial frequency, and its spatial heterogeneity resembles that of the eddy vorticity–gradient field. The deeper maximum departs from the characteristics anticipated by the YBJ approach. The dominant frequency at this level is twice the inertial frequency. The vertical velocity field associated with these superinertial waves is characterized by much smaller horizontal scales than at 100 m.

The existence of superinertial waves at 1700 m is important because they can potentially play a role in supplying energy to the universal internal wave field in the deep ocean and induce diapycnal mixing. Indeed the energy supplied by the lowest vertical normal modes with frequencies $\omega \geq 2f$ may subsequently be transferred to higher vertical modes and ultimately to small-scale mixing through parametric subharmonic instability (PSI; not taken into account in the present study) (MacKinnon and Winters 2005; Staquet and Sommeria 2002).

The emergence of double-inertial frequency waves in the deep interior at midlatitudes has already been reported (Niwa and Hibiya 1997; Price 1983) but in a very different physical context that concerns the ocean response to moving hurricanes. Niwa and Hibiya (1997) identified the generation mechanism of these waves as nonlinear interactions between higher vertical normal modes with frequency f producing lower modes with frequency $2f$. The efficiency of these interactions is strongly dependent on the hurricane size and propagation. In our study, the vertical-mode spectrum of near-

inertial waves, initially set up by the mixed layer depth, involves energy in both the lower and the higher modes, and these modes weakly interact at a later time (as anticipated by the YBJ approach for NIOs embedded in a mesoscale eddy field). Consequently, the generation mechanism of superinertial waves characterizing the lowest modes does not need to involve the higher modes and is therefore different from that of Niwa and Hibiya (1997). A plausible mechanism could be the nonlinear dynamics of the lowest vertical normal modes themselves. This generation mechanism is reported in a companion note (Danioux and Klein 2008).

The characteristics of the deep maximum of near-inertial vertical velocities, as well as the different mechanisms that explain it, reveal a pathway (driven by the eddy relative vorticity field) by which wind energy at midlatitudes quickly penetrates into the deep ocean interior. Both the amplitudes and characteristics of the vertical velocity field at such depths advocate further studies to fully evaluate the efficiency of the PSI mechanism (not taken into account in the present study) for transferring the corresponding energy to small-scale mixing.

Acknowledgments. This work is supported by the CNRS and IFREMER (FRANCE). Numerical simulations reported here were done at the IDRIS Orsay, France. We thank both reviewers for their comments.

APPENDIX

Analytical Solutions for the Vertical Velocity Using Young and Ben Jelloul's Approach

In this appendix, we derive an analytical expression for the inertial vertical velocity, which has never been done. We first summarize the derivation of the solution of (7)–(8) as performed in Klein et al. (2004), using YBJ's analytical approach. Because the eddy field is characterized by a continuous wavenumber spectrum, the integration of (7)–(8) in physical space is too difficult to treat exactly. An alternative is to work in Fourier space to obtain a solution for each wavenumber *k,* and then to come back to physical space. Using

$$X(x, y, t) = \sum_{p=-N}^{p=N} \sum_{q=-N}^{q=N} \hat{X}_{pq}(t) e^{i(px+qy)},$$

where X is any variable, $\hat{X}_{pq}$ is the Fourier transform of X, p and q are the horizontal wavenumbers, and N is the total number of horizontal Fourier modes, final solutions of (7)–(8) (subscript n related to the vertical mode number is removed for clarity) in spectral space are (Klein et al. 2004)

$$\frac{\hat{\mathcal{R}}'_k}{\mathcal{R}_0} = -\frac{T_k \hat{\zeta}_k}{4\pi}\left(1 - \cos\frac{2\pi t}{T_k}\right) \quad \text{and} \tag{A1}$$

$$\hat{\theta}'_k = -\frac{T_k \hat{\zeta}_k}{4\pi} \sin\frac{2\pi t}{T_k}, \tag{A2}$$

with $k^2 = p^2 + q^2$ and $T_k = 4\pi/(k^2 D)$. The D is the "dispersive" parameter defined as $r^2 f$, with r being the Rossby radius of deformation of the vertical normal mode considered. The consequence of (A1)–(A2) is that the amplitude and phase of the NIOs at a given wavenumber (or scale), that is, $\hat{\mathcal{R}}'_k$ and $\hat{\theta}'_k$, are directly linked to the eddy vorticity amplitude at the same wavenumber (or scale), that is, $\hat{\zeta}_k$. So when the eddy vorticity is characterized by a continuous wavenumber spectrum, the NIOs' field should be characterized as well by a continuous wavenumber spectrum, without invoking wave–wave interactions between NIOs. This property cannot be retrieved when the WKB assumption is invoked.

More specific properties of the NIOs' spectrum can be deduced from (A1)–(A2). Let us note k_0, the spectral peak of the vorticity, and focus on the spectral region corresponding to $k > k_0$. Assuming that the vorticity spectrum has a slope shallower than k^{-4}, (A1) indicates that $|\mathcal{R}'_k|$ is maximum for the wavenumber $k_c = \sqrt{2\pi/(Dt)}$. The $\hat{\mathcal{R}}'_k$ spectrum for $k \ll k_c$ has a positive slope and resembles the $\nabla^2\zeta$-spectrum. It can be approximated as $|\hat{\mathcal{R}}'_k|^2 \approx \mathcal{R}_0^2 (D^2/64) |\hat{\zeta}_k|^2 k^4 t^4$. This part of the spectrum increases with time proportional to t^4. For $k \gg k_c$, the $\mathcal{R}'$ spectrum has a steep negative slope, is steady, and resembles the streamfunction spectrum ($|\hat{\mathcal{R}}'_k|^2 \approx \mathcal{R}_0^2 |\hat{\zeta}_k|^2 D^{-2} k^{-4}$). Because the total near-inertial kinetic energy is equal to the integration of the $\mathcal{R}'$ spectrum over the wavenumber range, a simple calculation shows that the first part of the spectrum ($k < k_c$) is the dominant contribution. Then an estimation of the solution for $\mathcal{R}'$ in physical space can be derived by taking only the most energetic part of the spectrum, leading to the solution (11).

A solution for the near-inertial vertical velocity w can also be found using the YBJ approach. Let us find the expression of $\hat{w}_k$, the Fourier transform of $w = \partial u/\partial x + \partial v/\partial y$. Using $u + iv = (\mathcal{R}_0 + \mathcal{R}')e^{i(\theta_0 + \theta')}e^{-ift}$ and the solutions (A1)–(A2), we end up with the expression

$$\hat{w}_k = ik \frac{T_k \hat{\zeta}_k}{2\pi} \mathcal{R}_o \sin\frac{\pi t}{T_k} \sin\left[ft\left(1 + \frac{k^2 r^2}{4}\right) - \theta_o\right]. \tag{A3}$$

We focus on the subinertial part of $\hat{w}_k$, that is, the slow variation of its amplitude:

$$\hat{\mathcal{W}}_k = ik\frac{T_k\hat{\zeta}_k}{2\pi}\mathcal{R}_o \sin\frac{\pi t}{T_k}. \quad \text{(A4)}$$

At earlier times after the wind pulse, Eq. (A4) provides an approximate solution for w. If we assume $t \ll T_k$ for each wavenumber k, then $\hat{\mathcal{W}}_k = ik(\hat{\zeta}_k/2)\mathcal{R}_o t$, which means that the subinertial part $\mathcal{W}$ of w in physical space linearly increases with time and is close to the gradient of the eddy relative vorticity, that is,

$$\frac{\mathcal{W}}{\mathcal{R}_0} = \frac{t}{2}|\nabla\zeta|. \quad \text{(A5)}$$

The dominant frequency of w at these earlier times is [from (A3)] close to the Coriolis frequency.

At later times, (A4) implies a scale separation involving k_c such that, for $k < k_c$, the solution $\hat{\mathcal{W}}_k$ linearly increases with time and, for $k > k_c$, the solution oscillates around a steady value. Then, it is easy to show using the same arguments as for $\mathcal{R}'$ that the dominant part of the w spectrum concerns the spectral range $k < k_c$ and resembles the eddy vorticity gradient within this range, with its amplitude increasing linearly with time. In other words, the subinertial part of the vertical velocity field in physical space should match the eddy vorticity gradient field truncated so as to retain horizontal scales larger than $l_c = \sqrt{2\pi Dt}$. The analytical expression in physical space is

$$\frac{\mathcal{W}}{\mathcal{R}_0} = \frac{t}{2}|\nabla\zeta_c|, \quad \text{(A6)}$$

with $\nabla\zeta_c$ being the horizontal gradient of the vorticity field truncated so as to retain scales larger than $l_c = \sqrt{2\pi Dt}$. The dominant frequency of w at these later times is again close to the Coriolis frequency.

In terms of vertical normal modes, because D is smaller for the higher modes, the solution for $\mathcal{W}$ for these modes should still resemble (A5) after some inertial periods, that is, the total gradient of the relative vorticity field because of $t \ll T_k$. Another explanation is that $|\nabla\zeta_c| \approx |\nabla\zeta|$ and (A6) resembles (A5), because l_c is very small for these modes and because of the properties of the vorticity spectrum. On the other hand, the solution for $\mathcal{W}$ at that time for the lowest modes (with large D) should resemble (A6), that is, the gradient of the relative vorticity field truncated to retain scales larger than $l_c = \sqrt{2\pi Dt}$.

REFERENCES

Alford, M. H., 2003: Improved global maps and 54-year history of wind-work on ocean inertial motions. *Geophys. Res. Lett.,* **30,** 1424, doi:10.1029/2002GL016614.

Balmforth, N., S. L. Smith, and W. Young, 1998: Enhanced dispersion of near-inertial waves in an idealized geostrophic flow. *J. Mar. Res.,* **56,** 1–40.

Danioux, E., and P. Klein, 2008: A resonance mechanism leading to wind-forced motions with a 2*f* frequency. *J. Phys. Oceanogr.,* **38,** 2322–2329.

D'Asaro, E. A., 1989: The decay of wind-forced mixed layer inertial oscillations due to the β-effect. *J. Geophys. Res.,* **94,** 2045–2056.

——, 1995: Upper-ocean inertial currents forced by a strong storm. Part III: Interaction of inertial currents and mesoscale eddies. *J. Phys. Oceanogr.,* **25,** 2953–2958.

Flierl, G. R., 1978: Models of vertical structure and the calibration of two-layer models. *Dyn. Atmos. Oceans,* **2,** 341–381.

Garrett, C., 2001: What is the near-inertial band and why is it different from the rest of the internal wave spectrum. *J. Phys. Oceanogr.,* **31,** 962–971.

Gill, A. E., 1984: On the behavior of internal waves in the wakes of storms. *J. Phys. Oceanogr.,* **14,** 1129–1151.

Karsten, R., H. Jones, and J. Marshall, 2002: The role of eddy transfer in setting the stratification and transport of a circumpolar current. *J. Phys. Oceanogr.,* **32,** 39–54.

Klein, P., and A. M. Tréguier, 1995: Dispersion of wind-induced inertial waves by a barotropic jet. *J. Mar. Res.,* **53,** 1–22.

——, S. Llewellyn-Smith, and G. Lapeyre, 2004: Spatial organization of inertial energy by an eddy field. *Quart. J. Roy. Meteor. Soc.,* **130,** 1153–1166.

Kunze, E., 1985: Near-inertial wave propagation in geostrophic shear. *J. Phys. Oceanogr.,* **15,** 544–565.

Lapeyre, G., and P. Klein, 2006: Dynamics of the upper oceanic layers in terms of surface quasigeostrophy theory. *J. Phys. Oceanogr.,* **36,** 165–176.

Lee, D.-K., and P. P. Niiler, 1998: The inertial chimney: The near inertial energy drainage from the ocean surface to the deep layer. *J. Geophys. Res.,* **103,** 7579–7591.

MacKinnon, J., and K. B. Winters, 2005: Subtropical catastrophe: Significant loss of low-mode tidal energy at 28.9°. *Geophys. Res. Lett.,* **32,** L15605, doi:10.1029/2005GL023376.

Mellor, G. L., and T. Yamada, 1982: Development of a turbulence closure model for geophysical fluid problems. *Rev. Geophys. Space Phys.,* **851,** 851–875.

Metzger, M. M., 1999: Scalar dispersion in a two-dimensional random flow field. *Proc. Stirring and Mixing: 1999 Summer Study Program in Geophysical Fluid Dynamics,* Woods Hole, MA, Woods Hole Oceanographic Institution, 101–115.

Munk, W., and C. Wunsch, 1998: Abyssal recipes II: Energetics of tidal and wind mixing. *Deep-Sea Res.,* **45,** 1976–2009.

Niwa, J., and T. Hibiya, 1997: Nonlinear processes of energy transfer from traveling hurricanes to the deep ocean internal wave field. *J. Geophys. Res.,* **102,** 12 469–12 477.

Plougonven, R., and C. Snyder, 2005: Gravity waves excited by jets: Propagation versus generation. *Geophys. Res. Lett.,* **32,** L18802, doi:10.1029/2005GL023730.

Price, J. F., 1983: Internal wave wake of a moving storm. *J. Phys. Oceanogr.,* **13,** 949–965.

Rivière, P., A.-M. Tréguier, and P. Klein, 2004: Effects of bottom friction on nonlinear equilibration of an oceanic baroclinic jet. *J. Phys. Oceanogr.,* **34,** 416–432.

Staquet, C., and J. Sommeria, 2002: Internal gravity waves: From

instabilities to turbulence. *Annu. Rev. Fluid Mech.,* **34,** 559–593.

Straub, D. N., 2003: Instability of 2D flows to hydrostatic 3D perturbations. *J. Atmos. Sci.,* **60,** 79–102.

Van Meurs, P., 1998: Interactions between near-inertial mixed layer currents and the mesoscale: The importance of spatial variabilities in the vorticity field. *J. Phys. Oceanogr.,* **28,** 1363–1388.

Wunsch, C., and R. Ferrari, 2004: Vertical mixing, energy and the general circulation of the ocean. *Annu. Rev. Fluid Mech.,* **36,** 281–314.

Young, W. R., and M. Ben Jelloul, 1997: Propagation of near-inertial oscillations through a geostrophic flow. *J. Mar. Res.,* **55,** 735–766.

Zhai, X., R. Greatbach, and J. Zhao, 2005: Enhanced vertical propagation of storm-induced near-inertial energy in an eddying ocean channel model. *Geophys. Res. Lett.,* **32,** L18602, doi:10.1029/2005GL023643.